Journal of Glaciology, Vol. 48, *No.* 162, 2002

On the representation of ice-shelf grounding zones in SAR interferograms

Bernhard T. RABUS, Oliver LANG
German Remote Sensing Center (DFD), Oberpfaffenhofen, D-82234 Wessling, Germany
E-mail: bernhard.rabus@dlr.de

ABSTRACT. We investigate limitations of the one-dimensional elastic-beam model to detect grounding line and thickness of an ice shelf from a differential interferogram. Spatial limitations due to grounding-line curvature and variable ice thickness are analyzed by comparison with two-dimensional plate flexure. Temporal limitations from the tide-dependent shift of the grounding line are analyzed by superpositions of four tidal flexure profiles representing differential interferograms. (i) At scales greater than one ice thickness, seaward protrusions of the grounding line are well represented by the elastic-beam model, while landward embayments of the same scale produce significant misplacements >10% of the ice thickness. (ii) For reasonable spatial variations of shelf thickness, the elastic-beam model gives reliable estimates of grounding-line position and unfractured mean ice thickness near the grounding line. (iii) For about 20% of superpositions of four tidal flexure profiles, the resulting grounding-line misplacements exceed the physical tidal shift of the grounding line by factors >2. For differential tide levels <10% of a 1 m tide dynamics, a physical shift of the grounding line of 0.3 km per metre of tide can lever misplacements of >2 km. Examples of real interferometric profiles from West Antarctic ice shelves corroborate our results.

INTRODUCTION

The location of the grounding line on a tidewater glacier or ice shelf is immediately sensitive to changes in ice thickness and sea level (Hughes, 1977; Thomas, 1979). At constant sea level, repeat measurements of the grounding-line position can be used to monitor variations of ice flux or local mass-balance processes such as bottom melting. The grounding line is most accurately detected with an elastic ice model. This requires measurements of tidal uplift on a large spatial scale and on a long-term basis that became possible with space-borne synthetic aperture radar (SAR) interferometry (Goldstein and others, 1993; Rignot, 1998b). Besides other contributions such as topography, an interferogram of two SAR phase images acquired at different times measures surface motion towards the SAR sensor (Goldstein and others, 1993; Hartl and others, 1994). The ocean tides contribute a net vertical motion to the interferogram because they are generally incommensurable with the 24 hour repeat interval of available SAR satellites such as European Remote-sensing Satellite (ERS) or RADARSAT. Goldstein and others (1993) fitted the interferometrically measured tidal uplift along a profile perpendicular to the grounding line with the vertical displacement

$$w(x) = w_{\mathrm{msl}} + w_0\left\{1 - \mathrm{e}^{-\beta(x-x_{\mathrm{gl}})}[\cos\beta(x-x_{\mathrm{gl}}) + \sin\beta(x-x_{\mathrm{gl}})]\right\}, \quad x > x_{\mathrm{gl}} \qquad (1)$$

of an infinitely long beam, free floating on sea water and locked to bedrock beyond the grounding-line position[1] x_{gl}. Here, w_{msl} is the displacement corresponding to mean sea level, w_0 is the tide level, x is the distance along the profile, and β is the flexural parameter that depends on ice rheology and thickness. Rignot (1998a, b) extended this method to the difference of two interferograms. He showed that the actual grounding line x_{gl} could be detected reliably to better than 40 m if the grounding line was reasonably straight to justify the one-dimensional (1-D) treatment. The difference between detected and mean sea-level grounding line was estimated to be <300 m for his studied profiles.

In the present paper, we discuss the shortcomings of Equation (1) in a systematic and quantitative way. We distinguish between spatial (i) and temporal (ii) limitations of the 1-D model. The first are due to a non-zero curvature of the grounding line or a thickness variation along the profile. The second are due to the ephemeral migration of the grounding line as a function of the actual tide level. This migration effect is amplified in the difference interferogram, which contains a combination of four separate states of tidal uplift. For case (i) we calculate the flexure of a thin elastic plate for a specified grounding-line geometry, ice-thickness distribution and tide level. Equation (1), valid for a profile across a straight grounding line and constant ice thickness, is then used to recover the input values. Deviations from the input values are studied as a function of grounding-line curvature and ice-thickness distribution. For reasonable variations of ice thickness, these deviations are found to be small. Furthermore we show that profiles across convex sec-

[1] In reality x_{gl} is the position of the surface equivalent of the grounding line, the so-called hinge line, which differs slightly from the former as a function of ice thickness and maximum tidal uplift.

https://doi.org/10.3189/172756502781831197 Published online by Cambridge University Press

tions of the grounding line are generally much better represented by the 1-D model than profiles across concave sections of comparable curvature.

For case (ii) we use Equation (1) to calculate a series of four tide profiles corresponding to individual tide levels. The grounding-line position x_{gl} for the profiles is assumed to vary linearly with tide level. The quadruple difference of the profiles is used to simulate the representation of 1-D tidal flexure in a difference interferogram. The simulations are compared to examples of tidal uplift interferometrically measured at Pine Island and Thwaites Glaciers, West Antarctica. We show that for certain tidal combinations true and modelled grounding-line locations differ by up to several kilometres. Explicit knowledge of the tide levels (e.g. from a tide model) can be used to correct this effect.

TIDAL FORCING OF FLOATING AND GROUNDED ICE

Tidal forcing varies on hourly time-scales with amplitudes that are much smaller than the typical thicknesses of ice shelves and ice streams. Under these conditions, ice should behave as an elastic plate (e.g. Anandakrishnan and Alley, 1997, appendix A) that is buoyantly supported by ocean water below the grounding line and rests on bedrock or subglacial sediment above it. An immediate effect of the tidal forcing is vertical flexure of the floating ice as a so-called Kirchhoff plate clamped along the grounding line. This generalizes the flexure of an elastic beam to two dimensions and variable ice thickness.

One should mention that an elastic description of tidal flexure may not be generally valid. Lingle and others (1981) used a 1-D viscoelastic model to explain the tidal flexure across a lateral (i.e. flow-parallel) grounding line of Jakobshavn Isbræ, Greenland, that takes into account a suggested visco-plastic flexure of the bottom ice. In this paper we do not go beyond elastic flexure. We show, however, that deviations from the elastic-beam model observed for the Pine Island and Thwaites Glacier grounding zones, which can be explained with our model, cannot alternatively be explained with the viscoelastic model. We thus conclude that visco-plastic tidal flexure is not of importance there, but should be kept in mind when transferring our results to other grounding zones. Another important argument of Lingle and others (1981) is that flexure analysis, elastic or visco-plastic, must be restricted to the unfractured thickness of ice. Due to severe transverse crevassing, the equivalent elastic thickness of Jakobshavn Isbræ is $<20\%$ of the measured thickness. Using the same elastic parameters, we find a corresponding value of about 60% for Pine Island Glacier. In this paper, the terms "ice thickness" or "mean ice thickness" therefore always refer to the unfractured part of the ice column.

Besides vertical flexure, a possible second effect of the tidal forcing is damped waves of horizontal motion change that spread inland of the grounding line by a coupling of the ice to a layer of viscous basal till (Anandakrishnan and Alley, 1997). Such waves with a velocity of about $1.6\,\mathrm{m\,s^{-1}}$ were traced indirectly from seismicity time series on Ice Stream C up to 85 km from the grounding line. Besides till deformation, there are two other accepted mechanisms of fast ice motion, basal sliding and deformation of soft basal ice (Smith, 1997). While tidal forcing seems to have no effect where ice motion is dominated by the latter mechanism, forced variations of basal water pressure could theoretically give rise to similar waves of sliding variation (Echelmeyer and Harrison, 1989).

A central issue is whether these horizontal motion changes can be misinterpreted as vertical flexure in an interferogram, therefore contaminating the information on the location of the grounding line. Because Ice Stream C is almost stagnant, maximum horizontal motion changes in the vicinity of the grounding line are only around $1\,\mathrm{mm\,d^{-1}}$, which is clearly irrelevant for interferograms with short temporal baseline. Newer results on fast-moving Ice Stream D (personal communication from S. Anandakrishan, 2001) suggest, however, considerably larger tidal velocity variations up to several tens of centimetres per day. The interferometric contribution will be significantly reduced due to generally similar tides for the two SAR acquisitions, separated by a multiple of 24 hours. Maximum contributions consequently should be <10 cm (~1 fringe for ERS tandem). The spatial characteristics of motion change on Ice Stream C suggest that the net effect on the interferometric representation of the ice-shelf grounding zone is the addition of an almost linear phase ramp. This is because the observed wave velocity translates into a wavelength of 70 km, which is much longer than the width of the grounding zone (a few kilometres). Thus, we rule out temporal variations of horizontal motion as a source of error.

The vertical flexure $w(x, y)$ of an ice shelf is described by the fourth-order partial differential equation (Kirchhoff, 1850),

$$\mathbf{K}D\mathbf{C}\mathbf{K}^T w + \rho_w g w = 0\,, \tag{2}$$

with

$$\mathbf{C} = \begin{bmatrix} 1 & \nu & 0 \\ \nu & 1 & 0 \\ 0 & 0 & \frac{1-\nu}{2} \end{bmatrix} \quad D = \frac{Eh^3}{12(1-\nu^2)}\,,$$

$$\mathbf{K} = \left[\frac{\partial^2}{\partial x^2} \frac{\partial^2}{\partial y^2} 2\frac{\partial^2}{\partial x \partial y}\right]$$

being the elasticity matrix of an isotropic material, the flexural rigidity and the curvature differential operator, respectively; ρ_w is the density of sea water, and g is the Earth gravity acceleration. The flexural rigidity depends on thickness h, as well as elastic properties, Young's modulus E and Poisson ratio ν. The respective boundary conditions at the grounding line (gl) and at infinite seaward distance from the grounding line (∞) are

$$\left.\frac{\partial w}{\partial x}\right|_{gl} = \left.\frac{\partial w}{\partial y}\right|_{gl} = w\Big|_{gl} = 0 \quad \text{and} \quad w\Big|_{\infty} = w_0\,. \tag{3}$$

The boundary condition at the grounding line corresponds to zero vertical flexure of all grounded ice. For the subglacial conditions of bed deformation or sliding discussed before, there is the theoretical possibility of incomplete locking of the grounded ice landward of the grounding line. In this case, the corresponding boundary conditions would not require a zero derivative of tidal flexure at the grounding line as in Equation (3), and we would get a damped extension of vertical tidal flexure up-glacier of the grounding line. This extension is not described by Equation (1) even for a straight grounding line and constant ice thickness. As opposed to the tidally forced waves of horizontal motion change discussed before, the vertical flexure of grounded ice creates a volume-conservation problem that can only be solved by large-scale redistribution of sea water and/or till between subglacial areas above the grounding line on the time-scale of hours

https://doi.org/10.3189/172756502781831197 Published online by Cambridge University Press

(see also discussion in Anandakrishnan and Alley, 1997). The physical feasibility of such a mechanism is unlikely and we do not address potential limitations due to this type of modified boundary condition in the paper.

SPATIAL LIMITATIONS OF THE ELASTIC-BEAM MODEL

Equation (2) describes vertical flexure for the general two-dimensional (2-D) case for non-constant D, i.e. the grounding line can be arbitrarily curved and thickness and/or elastic properties of the ice shelf can be spatially variable. In this paper, we investigate several special cases of Equation (2) that are tabulated in Table 1 together with their corresponding numerical solution methods. The flexural parameter β is defined in the table; β^{-1} defines a characteristic scale for the horizontal coordinates; in most of the analysis we consequently use dimensionless coordinates such as βx, βy. Dimensionless coordinate values can be read directly in kilometres for an ice thickness of about 700 m because $\beta \approx 1\,\mathrm{km}^{-1}$ in this case.

For each case of Table 1 we fit Equation (1) to the calculated tidal flexure to obtain the dimensionless grounding-line misplacement, ice-thickness bias, and tide-level bias of the elastic-beam model. Two sources contribute to the error budget of these parameters. The first is the error from the numerical integration of the appropriate differential equation. The second error source results from the fit process. Using the fit statistics, this latter error was evaluated to be $<10^{-3}$ for all experiments presented in the paper. For the 1-D numerical solution methods (cases II–IV in Table 1) the first error source is several orders of magnitude smaller than the second. Thus the overall error is estimated to be 10^{-3} in this case. To estimate the overall error for the finite-element case (V in Table 1) we compared the calculated dimensionless parameters for a grounding line with zero or constant curvature, with the corresponding parameters calculated for the 1-D cases. These tests showed that the overall error is better than 10^{-2} for the finite-element case.

1-D flexure with constant ice thickness (I): effects of profile misalignment

As shown in Table 1, Equation (1) already is the proper solution. However, this simple case allows one to investigate the effects of fitting Equation (1) to a flexure profile that is not perpendicular to the grounding line but is misaligned by an angle α. This is relevant to real data, where choosing profiles perpendicular to an (a priori unknown) grounding line will always introduce directional errors up to some 10°. The sensitivity of the fit parameters w_0, β and x_{gl} is analytically evaluated by noting that the distance along such a misaligned profile is given by $s = x(\cos\alpha)^{-1}$. Replacing x by $s\cos\alpha$ in Equation (1) immediately shows that w_0 and $x_{\mathrm{gl}} = s_{\mathrm{gl}}\cos\alpha$ are unaffected, while β is replaced by $\beta\cos\alpha$. We conclude that for a reasonably straight grounding line, ice thickness h obtained by fitting Equation (1) is overestimated by a factor $(\cos\alpha)^{-3/4}$. For a misalignment of $\alpha = 10°$ this positive bias is $<5\%$; for $\alpha = 20°$ it is about 11%.

1-D flexure with variable ice thickness (II)

Most ice shelves show a seaward reduction of ice thickness, controlled by the spatial distributions of local mass balance and ice velocity on the shelf (Paterson, 1994, p. 300, equation 42). To our knowledge, there is no agreed mathematical shape of a typical shelf-ice thickness profile. Published profiles (e.g. Crabtree and Doake, 1982; Allen and others, 1997) usually show a monotonic decrease of the absolute value of the ice-thickness gradient with distance from the grounding line. This characteristic is approximated by a simple exponential thickness profile

$$\frac{h(x)}{h_{\mathrm{gl}}} = R_{\mathrm{fi}} + (1 - R_{\mathrm{fi}})\exp\left(-\frac{x}{x_{\mathrm{dec}}}\right). \qquad (4)$$

Here, R_{fi} is the ratio of minimum ice thickness at the shelf edge to maximum ice thickness h_{gl} at the grounding line; x_{dec} is a characteristic length that determines the ice-thickness gradi-

Table 1. Special cases of Equation (2): descriptions, differential equations and solution schemes

Case	*Grounding line*	*Ice thickness h*	*Differential equation*	*Solution*
I	Straight along y axis	constant	$\frac{\partial^4}{\partial x^4}w + 4\beta^4 w = 0$	Analytical: Equation (1)
II	Straight along y axis	variable	$\frac{1}{h_{\mathrm{gl}}^3}\frac{\partial^2}{\partial x^2}h^3\frac{\partial^2}{\partial x^2}w + 4\beta^4 w = 0$	Numerical: Runge–Kutta
III	Constant curvature (circle)	constant	$\left(\frac{\partial^2}{\partial r^2}+\frac{1}{r}\frac{\partial}{\partial r}\right)\left(\frac{\partial^2}{\partial r^2}+\frac{1}{r}\frac{\partial}{\partial r}\right)w + 4\beta^4 w = 0$	Numerical: Runge–Kutta
IV	Constant curvature (circle)	variable	$\frac{1}{h_{\mathrm{gl}}^3}\left(\frac{\partial^2}{\partial r^2}+\frac{1}{r}\frac{\partial}{\partial r}\right)h^3\left(\frac{\partial^2}{\partial r^2}+\frac{1}{r}\frac{\partial}{\partial r}\right)w + 4\frac{\nu-1}{h_{\mathrm{gl}}^3 r}\left(\frac{\partial h^3}{\partial r}\frac{\partial w}{\partial r}\right) + 4\beta^4 w = 0$	Numerical: Runge–Kutta
V	Curved	constant	$\Delta\Delta w + 4\beta^4 w = 0$	Numerical: 2-D finite element

Definitions:

flexural parameter: $\beta = \left[3(1-\nu^2)\rho_{\mathrm{w}}g\right]^{\frac{1}{4}}E^{-\frac{1}{4}}h_{\mathrm{gl}}^{-\frac{3}{4}}$

Laplacian (Cartesian coordinates): $\Delta = \frac{\partial^2}{\partial x^2}+\frac{\partial^2}{\partial y^2}$

polar coordinates: $r = \sqrt{x^2+y^2}, \quad \varphi = \tan^{-1}\left(\frac{y}{x}\right)$

Parameter values: $\rho_{\mathrm{w}} = 1000\,\mathrm{kg\,m^{-3}}$, $\rho_{\mathrm{i}} = 900\,\mathrm{kg\,m^{-3}}$, $g = 9.8\,\mathrm{m\,s^{-2}}$, $E = 9\times10^6\,\mathrm{N\,m^{-2}}$, $\nu = 0.33$

https://doi.org/10.3189/172756502781831197 Published online by Cambridge University Press

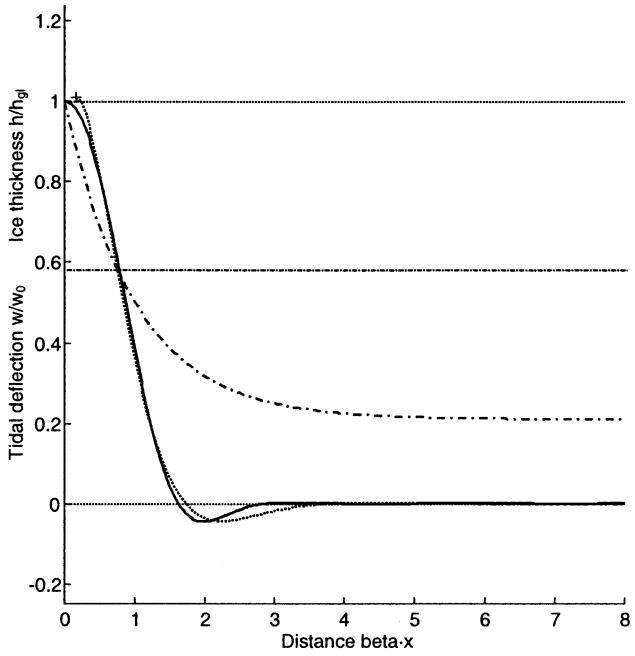

Fig. 1. Flexure of a 1-D beam with variable thickness (solid line) compared to the Equation (1) best fit (dotted line). Also shown are the variable thickness parameterized by $R_{\mathrm{fi}} = 0.2$, $\beta x_{\mathrm{dec}} = 1$ (dash-dotted line), as well as the constant thickness $h^{\mathrm{fit}}/h_{\mathrm{gl}} = 0.58$ (dashed line) and the resulting grounding-line misplacement $\beta(x_{\mathrm{gl}}^{\mathrm{fit}} - x_{\mathrm{gl}}) = 0.16$ (cross symbol) of the fit.

ent. Equation (4) is used in the following to quantify the effect of variable ice thickness on the profile of tidal flexure.

Figure 1 shows a concrete example with $R_{\mathrm{fi}} = 0.2$ and $\beta x_{\mathrm{dec}} = 1$. For $h_{\mathrm{gl}} = 700$ m these parameters correspond to an ice shelf whose ice thickness drops to less than half within 1 km of the grounding line. Thickness gradients of this size are not what is typically observed. However, even for this extreme case the flexure profile does not deviate substantially from the simple flexible-beam model. For $h_{\mathrm{gl}} = 700$ m the resulting fit corresponds to an equivalent constant ice thickness $h^{\mathrm{fit}} = 406$ m calculated from the fitted flexural parameter $\beta^{\mathrm{fit}}/\beta$. The grounding line is misplaced seaward by 160 m due to the reduced flexure near the grounding line, where the ice is thicker than h^{fit}. The biases of the parameters fitted with Equation (1) are presented in Figure 2 for a wide range of R_{fi} and βx_{dec} values. Figure 2a shows the grounding-line misplacement $\beta(x_{\mathrm{gl}}^{\mathrm{fit}} - x_{\mathrm{gl}})$, Figure 2b shows the tide-level bias $w_0^{\mathrm{fit}}/w_0 - 1$, and Figure 2c shows the corresponding bias of the (constant) ice thickness $h^{\mathrm{fit}}/h_{\mathrm{av}} - 1$. The latter is calculated relative to an average ice thickness h_{av} that is representative of the belt of strong tidal flexure between the grounding line and the "forebulge" of the flexure profile, where $\partial w/\partial x = 0$. We calculate h_{av} by averaging Equation (4) over the interval $[0, \pi(\beta^{\mathrm{fit}})^{-1}]$. The misplacement of the grounding line is generally smaller than $0.2\beta^{-1}$, and the fitted tide level is accurate to within 1%; fitted and average ice thickness agrees to within 10%.

Our analysis applies qualitatively to spatial thickness variations more general than Equation (4). For a profile across a real ice shelf we expect Equation (1) to produce an accurate measurement of tide level, as well as an estimate (on the 10% level) of mean ice thickness averaged over the belt of strong tidal flexure. At the same time, grounding-line location is misplaced (seaward for negative, and landward for positive ice-thickness gradient) on the order of 10% of the ice thickness.

2-D flexure with constant ice thickness and circular grounding line (III)

Next, we discuss the 2-D flexure of an ice shelf for the special case that the grounding line is a circle of radius r_{gl}. By introducing polar coordinates (see Table 1) Equation (2) reduces to an ordinary differential equation with the independent vari-

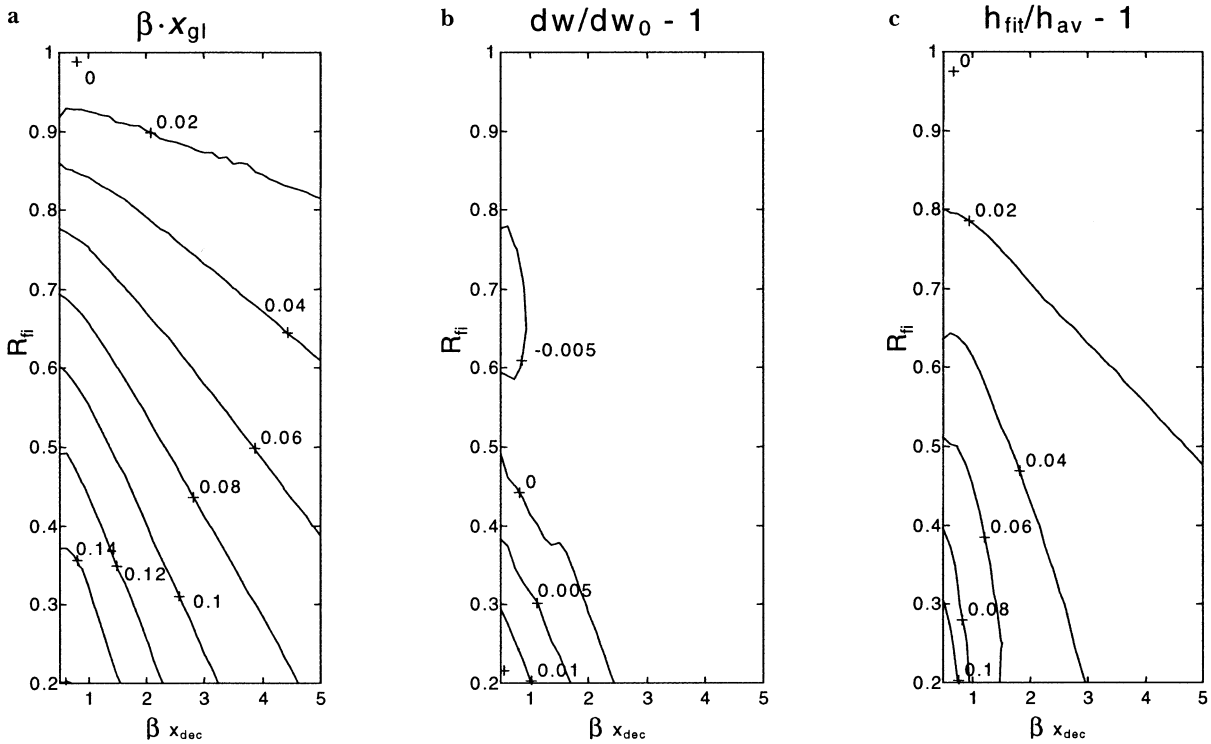

Fig. 2. Parameters fitted with Equation (1) for shelf-ice thickness distributions described by Equation (4). Shown are (a) grounding-line misplacement, (b) fractional difference between fitted and input tidal amplitudes, and (c) fractional difference between fitted and average ice thickness. Here, the average h_{av} is taken from the grounding line ($x = 0$) out to $x = \pi(\beta^{\mathrm{fit}})^{-1}$.

https://doi.org/10.3189/172756502781831197 Published online by Cambridge University Press

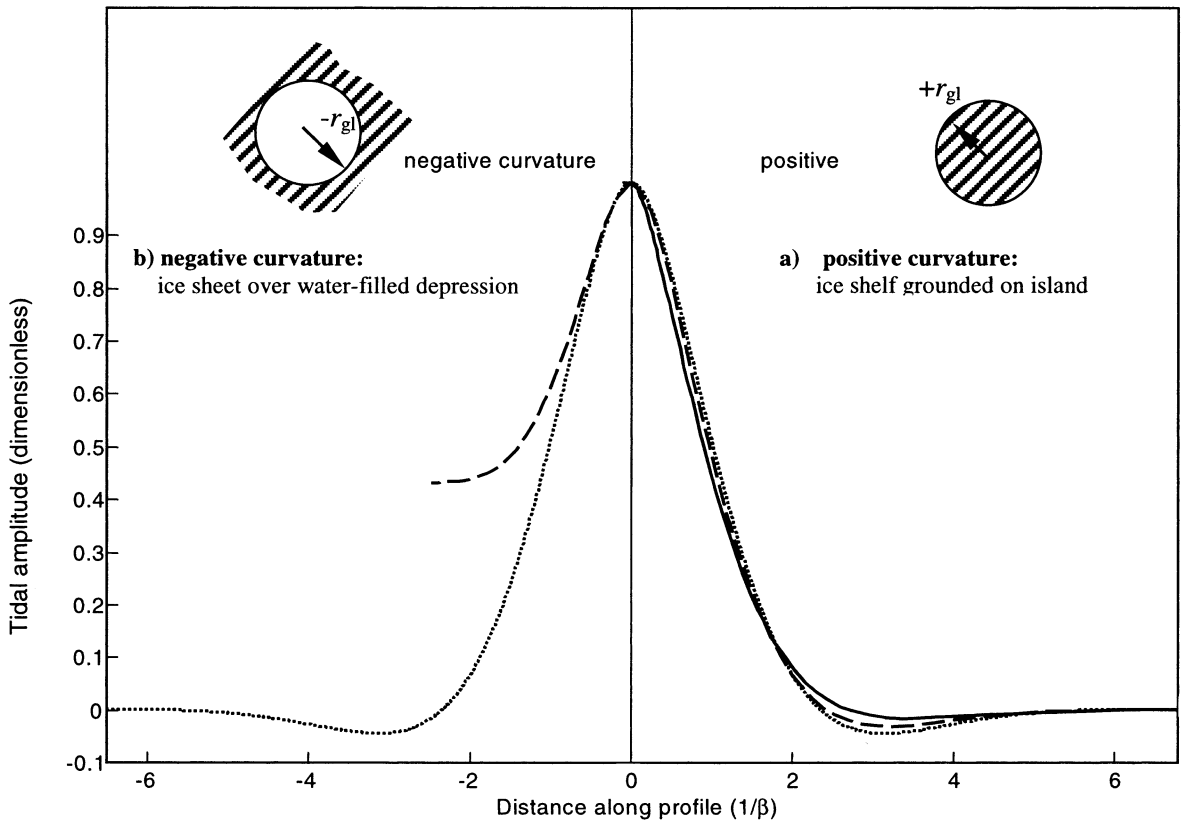

Fig. 3. The two sub-cases of 2-D flexure of an ice sheet over a circular grounding line. Sketch maps: the ice cover over the hatched areas is grounded; over the white areas it is floating. Graph: Corresponding to the sketch maps we show examples of flexure profiles for convex (positive curvature) and concave (negative curvature) grounding line with $r_{gl} = \pm\infty$ (dotted line), $2.5\beta^{-1}$ (dashed line), $0.05\beta^{-1}$ (solid line).

able r. Figure 3 shows that there are two qualitatively different sub-cases with convex $(+r_{gl}^{-1})$ and concave $(-r_{gl}^{-1})$ curvature, respectively. Sub-case (a) represents an ice shelf resting on a disc-shaped island, while (b) represents an ice sheet grounded everywhere except where it overlays a circular water-filled depression (e.g. a subglacial lake subject to fluctuations of its water level). A comparison of the characteristics of the two sub-cases is important for understanding the flexure across a grounding line of more general shape consisting of sections of (variable) positive and negative curvature (case V, discussed later). Sub-case (a) is similar to cases I and II, in that the second of the boundary conditions in Equation (2) is analogously

$$w(r \to \infty) = w_0\,. \tag{5}$$

This gives a so-called outer solution of the differential equation of case III. Corresponding flexure profiles for different radii of curvature are shown in Figure 3 (right side). With decreasing r_{gl} the flexure gradient in the vicinity of the grounding line increases. On the other hand, the characteristic forebulge of the flexure profile shows a decrease in height as well as a seaward shift in location.

For sub-case (b) we must look for an inner solution of the differential equation that reaches from $r = r_{gl}$ to $r = 0$. Here, the corresponding second boundary condition is

$$\frac{\partial w}{\partial r}(r \to 0) = 0\,. \tag{6}$$

For small r_{gl} on the order of β^{-1} we generally find $w(r = 0) \neq w_0$ for the flexure at the centre of the circle, i.e. the ice sheet does not reach complete isostatic balance there. This effect is seen for the flexure profiles shown on the left side of Figure 3. Case V will show that on a small scale, landward embayments of the grounding line correspond to the inner solution of sub-case (b), while seaward protrusions of the grounding line correspond to sub-case (a). With increasing distance from the grounding line, these small-scale solutions merge into a large-scale solution, which always resembles an outer solution of the type of case I. As a consequence, landward embayments, which require the merging of qualitatively different small- and large-scale solutions, are poorly described by the flexible-beam model.

For sub-case (a), grounding-line misplacement $\beta(r_{gl}^{fit} - r_{gl})$, ice-thickness bias $h^{fit}/h - 1$, and tide-level $w_0^{fit}/w_0 - 1$ for a range of curvature (r_{gl}^{-1}) are shown in Figure 4. Grounding-line misplacement is always landwards; for curvatures in the range $10–20\beta$ it reaches maximum negative values around $-0.25\beta^{-1}$. Ice-thickness and tide-level biases reach corresponding positive maxima of 5% and 15%, respectively. The enhanced flexure for a curved grounding line should lead to a negative ice-thickness bias. The observed positive bias can be explained by an overcompensation by the other two fit parameters. Figure 4b shows a negative ice-thickness deviation up to −10% if grounding-line location and tide level are kept fixed at their exact values.

2-D flexure with variable ice thickness and circular grounding line (IV)

As for case III, we use polar coordinates. We assume a thickness variation with radial symmetry described by Equation (4) with the independent variable r instead of x. Radial profiles of 1-D flexure are found by solving the resulting ordinary differential equation in Table 1. The biases of

https://doi.org/10.3189/172756502781831197 Published online by Cambridge University Press

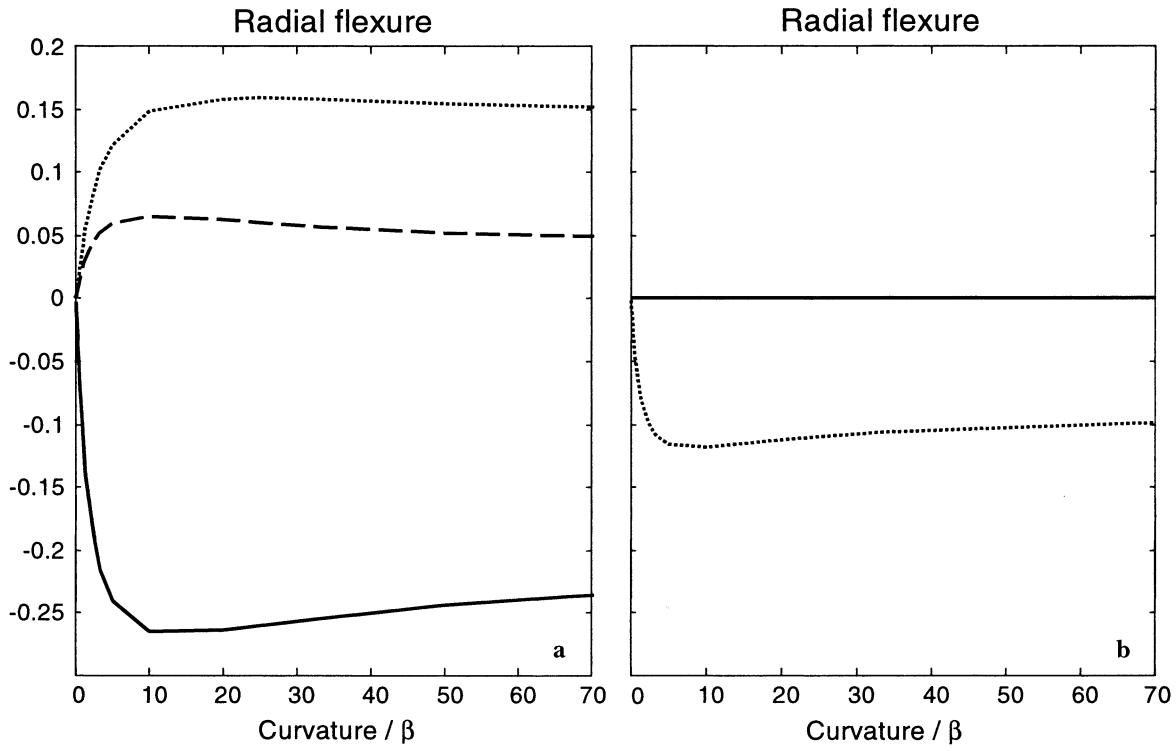

Fig. 4. Parameters fitted with Equation (1) for case IIIa as a function of grounding-line curvature. Shown are deviations with respect to the exact values; grounding-line position (solid line), tide level (dashed line), ice thickness (dotted line). (a) All parameters are fitted; (b) only ice thickness is fitted, while grounding-line position and tide level are fixed at their respective exact values.

grounding-line position, ice thickness and tide level will be a combination of those of cases II and III. We only discuss the sub-case of a convex grounding line ($r_{\mathrm{gl}}^{-1} > 0$). We assume the combined biases to be small for this case, and consequently do not calculate them for the entire parameter ranges of r_{gl}^{-1}, R_{fi}, r_{dec} taken from Figures 2 and 4. Instead we choose only two combinations ($\beta r_{\mathrm{gl}}^{-1}$, R_{fi}, βr_{dec}) = (2.0, 0.5, 1.0) and (10.0, 0.2, 0.5), with moderate and extreme values, respectively, to check our assumption. The grounding-line misplacement for the first combination is $\beta(r_{\mathrm{gl}}^{\mathrm{fit}} - r_{\mathrm{gl}}) = -0.01$, which compares to individual misplacements of +0.11 and −0.17 for cases II and III, respectively. For the second combination we find +0.09, which compares to +0.16 and −0.26 for the individual misplacements. The combined ice-thickness bias is very similar to that of case II. We conclude that misplacement of a convex grounding line is partially compensated by a seaward decrease of shelf-ice thickness.

2-D flexure with constant thickness and grounding line of arbitrary curvature (V)

Equation (2) for constant ice thickness is solved with the finite-element method on a 2-D xy domain bounded by the grounding line on the left side (Fig. 5a and b). The accuracy of the method was verified by using a straight grounding line along the y axis and comparing the solution with Equation (1). As an example of a grounding line with variable curvature we use a Gaussian shape that merges into the y axis on the upper and lower side to allow for boundary conditions corresponding to a straight grounding line there. We investigate two sub-cases: (i) a "Gaussian protrusion", where curvature changes symmetrically from a central positive maximum to a smaller negative minimum and back to zero, and (ii) a Gaussian embayment with the sign of curvature reversed everywhere. For sub-case (i), Figure 5a and b show the calculated tidal flexure displayed as interferometric fringe patterns for two concrete examples of small and large shelf thickness. In contrast to the previous analysis, we use dimensional coordinates for case V.

As in cases II–IV, we find the effective grounding-line position and ice thickness corresponding to the elastic-beam model by fitting profiles of 2-D flexure perpendicular to the (true) grounding line. For sub-case (i), Figure 5c shows the effective grounding line for different ice thickness; Figure 5d shows corresponding results for sub-case (ii). For ice thickness much smaller than the radius of curvature, detected and true grounding line agree. For thicker ice, the effective grounding line becomes a diffused image of the true grounding line in sub-case (i). The corresponding grounding-line misplacement is systematic and predictable. In sub-case (ii), the result is very different. Here, the grounding-line misplacement is generally larger and of more complicated shape even for comparatively small ice thickness. For very large ice thickness both sub-cases are alike again. The detected grounding line becomes straight, bridging the "embayment"-, and cutting off the "protrusion"-type excursion of the true grounding line, respectively.

In Figure 6 we plot βy against dimensionless grounding-line misplacement, ice-thickness bias and tide-level bias of sub-case (i). The results show that case III can be generalized to a grounding line of variable curvature. As expected from the discussion of case III, the grounding-line misplacement varies with curvature and is over-proportionally large at the flanks of the protrusion, where the curvature is negative. As for case III, ice-thickness counter-intuitively is overestimated for positive curvature due to the compensating influence of grounding-line misplacement. In summary, embayments of the grounding line whose spatial scales are comparable to the ice thickness or smaller cannot be fitted reliably with Equation (1). In contrast, protrusions of the same scale produce comparatively small grounding-line misplacement that can be corrected approximately.

https://doi.org/10.3189/172756502781831197 Published online by Cambridge University Press

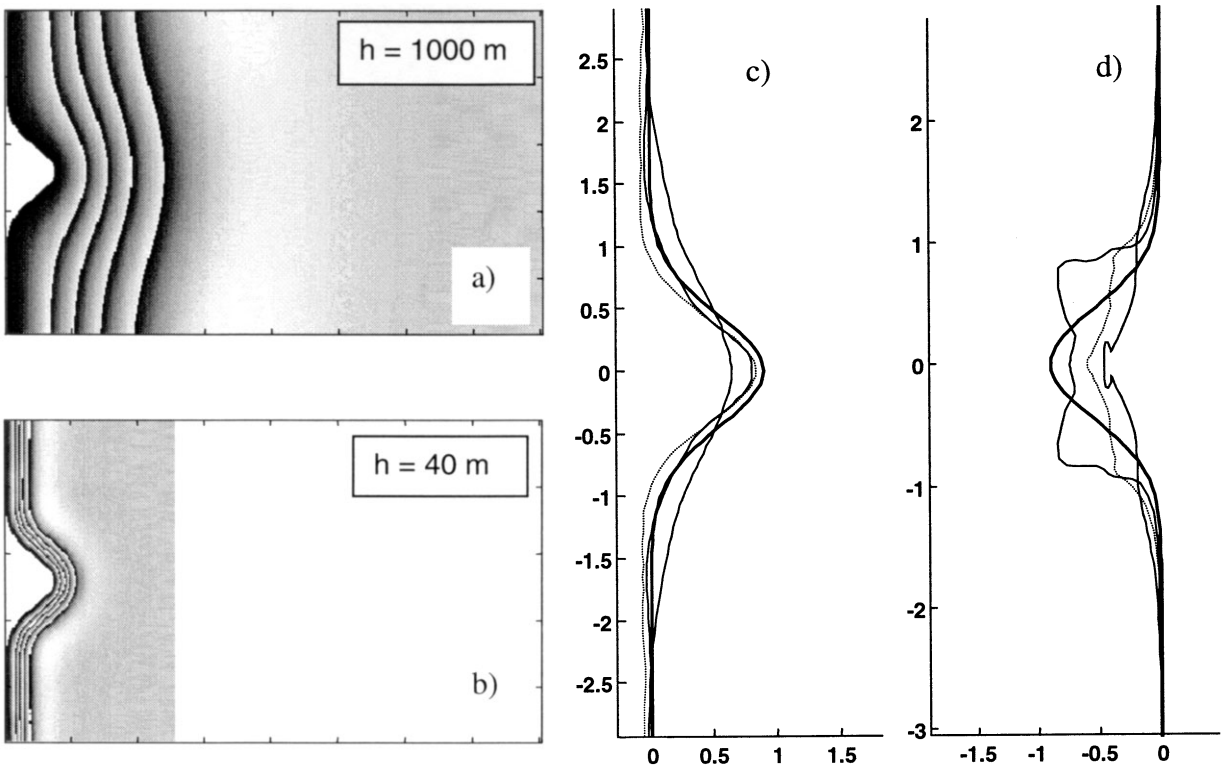

Fig. 5. Left panel: 2-D flexure of an ice shelf of constant thickness over a Gaussian-shaped grounding line: (a) 1000 m, (b) 40 m. Right panel: grounding-line displacement: (c) Gaussian protrusion, (d) Gaussian bay for ice shelves of various thicknesses (40, 250, 500, 1000 m); x, y coordinates in km.

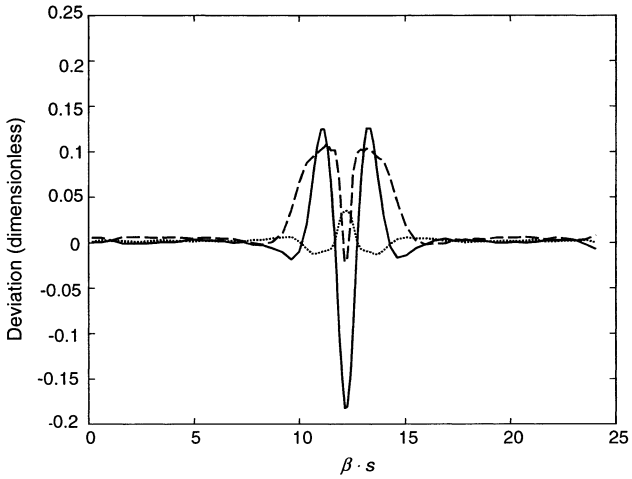

Fig. 6. 2-D flexure of constant-thickness ice shelf over Gaussian protrusion (Fig. 5a) fitted with Equation (1). Shown are: grounding-line displacement (solid line), beta (dashed line) and tide level (dash dotted line).

TEMPORAL LIMITATIONS OF THE ELASTIC-BEAM MODEL

For straight to moderately convex stretches of the grounding line, absolute biases of grounding-line location are small (typically <100 m) and they will largely cancel during the evaluation of relative grounding-line changes. Nevertheless, the corresponding phase contribution of tidal motion in a differential interferogram can deviate significantly from Equation (1). The reason is the temporal superposition of four individual patterns of tidal flexure. These patterns are shifted relative to each other because the actual grounding-line location fluctuates with the tide level (Rignot, 1998b). In regions that show ephemeral fluctuations on the order of a few hundred metres per metre of tide, the grounding line detected with Equation (1) can be misplaced by several kilometres. The resulting misplacement depends on the particular combination of tide levels. The effect is important to consider since it is exactly these regions, where the grounding line is sensitive to tide level, or alternatively to small changes in shelf-ice thickness, that are interesting to monitor from a climatological and ice-dynamical standpoint. In this section, we model quadruple-difference profiles of tidal flexure for a straight grounding line and compare the results to real data from Thwaites and Pine Island Glaciers.

In the following, S_2 and S_4 denote the difference operators describing the formation of single and differential interferograms, respectively. Applying S_4 to Equation (1) yields

$$S_4(w_i) = (w_1 - w_2) - (w_3 - w_4) \tag{7}$$
$$= S_4\big[\Delta w_i\big(1 - \mathrm{e}^{-\beta(x-x_{\mathrm{msl}})}\,\mathrm{e}^{\beta f \Delta w_i}\big\{\cos\big[\beta(x - x_{\mathrm{msl}} - f\Delta w_i) + \sin(\beta(x - x_{\mathrm{msl}} - f\Delta w_i)\big]\big\}\big)\big]\,, \qquad x > \max(f\Delta w_i)\,.$$

Here, x_{msl} is the grounding-line location at mean sea level w_{msl}; without loss of generality we set $x_{\mathrm{msl}} = w_{\mathrm{msl}} = 0$ in subsequent calculations. By Δw_i we denote the four tide levels at the acquisition times of the individual SAR scenes, and we have introduced the rate $f = \Delta x_{\mathrm{gl}}/\Delta w$ of grounding-line shift Δx_{gl} with tide level Δw. According to Rignot (1998b),

$$f = \frac{1}{\alpha_{\mathrm{s}} - \alpha_{\mathrm{b}}(1 - \rho_{\mathrm{w}}/\rho_{\mathrm{i}})}\,, \tag{8}$$

with α_{s} and α_{b} being surface and bed slope, respectively. Equation (7) is valid for $x > \max(f\Delta w_i)$ when all four SAR scenes cover floating ice. For $x < \min(f\Delta w_i)$ there is no tidal contribution to the differential interferogram because the ice is grounded in all scenes. In the range $\min(f\Delta w_i) < x < \max(f\Delta w_i)$ we pass the sequence of actual grounding lines in the order of the respective tide levels of the SAR scenes. Here, the tidal phase contribution

https://doi.org/10.3189/172756502781831197 Published online by Cambridge University Press

is formed by the superposition of three, then two, and finally only one, individual flexure profile. The resulting deviation of the interferometric profile from Equation (7) close to the mean sea-level grounding line x_{msl} is demonstrated later.

Equation (7) can be rearranged as

$$S_4(w_i) = S_4(\Delta w_i)\left[1 - \mathrm{e}^{-\beta x}(A\cos\beta x + B\sin\beta x)\right] \quad (9)$$

with

$$A = \frac{1}{S_4(\Delta w_i)} S_4\left[\Delta w_i \mathrm{e}^{-\beta f \Delta w_i}(\cos\beta f\Delta w_i + \sin\beta f\Delta w_i)\right]$$
$$B = \frac{1}{S_4(\Delta w_i)} S_4\left[\Delta w_i \mathrm{e}^{-\beta f \Delta w_i}(\cos\beta f\Delta w_i - \sin\beta f\Delta w_i)\right]. \quad (10)$$

For cases where the expression $\beta f \Delta w_i$ is small, Equations (10) can be linearly approximated according to

$$A = 1\,, \quad B = 1 + 2\beta f \frac{S_4(\Delta w_i^2)}{S_4(\Delta w_i)}\,. \quad (11)$$

Finally, Equation (9) can be recast into the form of Equation (1) by introducing

$$\Delta x_{\mathrm{gl}} = \frac{1}{\beta}\arctan\left(\frac{1-\frac{B}{A}}{1+\frac{B}{A}}\right), \quad w_0 = S_4(\Delta w_i)\sqrt{\frac{A^2+b^2}{2}}, \quad (12)$$

as grounding-line misplacement $\Delta x_{\mathrm{gl}} = x_{\mathrm{gl}} - x_{\mathrm{msl}}$ and tidal amplitude, respectively. A profile in a differential interferogram consequently has the same shape as a single tidal profile but is shifted and stretched according to Equations (12). Reliable detection of the grounding-line location in differential interferograms with Equation (1) generally requires $A \approx B$. Otherwise, grounding-line misplacements of up to $(\pi/2)\beta^{-1}$ are possible. For an ice shelf about 1000 m thick ($\beta = 0.6\,\mathrm{km}^{-1}$) maximum misplacement is about 2.5 km.

In the following we evaluate the conditions and statistical probability for large values of Δx to occur in a differential interferogram. We use FES95.2 (Le Provost and others, 1998), a global finite-element hydrodynamic model improved by TOPEX/POSEIDON altimeter data, to create a time series of quadruple tidal differences $S_4(w_i)$. We apply the model to a location near Thwaites Glacier over a time-span of 2 years (1 March 1996 to 1 March 1998). The simulated differences of acquisition time for the single interferograms were 1 day (ERS tandem mission). For the time difference between two single interferograms that form a differential interferogram we used 35 days (one repeat cycle). Individual tide levels of the time series range between −0.2 and 0.97 m.

The statistical frequency distribution for double $S_2(w_i)$ and quadruple $S_4(w_i)$ tidal differences is shown in Figure 7a and b, respectively. The corresponding grounding-line misplacement Δx_{gl}, from Equations (12) is shown in Figure 7c. For the simulation we have chosen $\beta = 0.6\,\mathrm{km}^{-1}$ and $f = 300$. In Figure 7d the simulated grounding-line misplacements and quadruple differences are plotted against each other. The latter plot shows that $S_4(w_i) < 0.1$ m is a necessary condition for large Δx_{gl}. From Figure 7c we find a 20% probability for Δx_{gl} to exceed the expected range of grounding-line shift with tide level by factors larger than two.

Tests show that, for the given geographic region, FES95.2 fails to reproduce particular quadruple tidal differences measured in differential interferograms. However, our analysis is not sensitive to these individual prediction errors. The only necessary assumption is that the internal statistics of the simulated time series of individual tide levels is realistic. The dynamics of the simulated tide series is considered a lower bound to realistic tide-level variations. Channel effects caused by the geometry of the coastline as well as the bathymetry in the vicinity of the grounding line are known to amplify the tide dynamics considerably (Kertz, 1992). Direct measurements of tide dynamics from other ice-shelf areas of Antarctica (e.g. 6 m at Ronne Ice Shelf (Doake, 1992) and 1.8 m at Schirmacheroasen (Metzig, 1997)) also suggest that our simulation may underestimate the tide dynamics. A more realistic modelled tide dynamics would produce more data points with substantial misplacement Δx_{gl} for large $S_4(w_i)$.

The profiles with very large Δx_{gl} on the order of several kilometres all show strong deviations with respect to the flexure of an elastic beam locked at the true grounding line. There are, however, two subjective categories of large Δx_{gl}, depending on whether it is nevertheless possible to identify the approximate location of the true grounding line by eye or not. In Figure 8 the two categories are illustrated with examples of real data, from Pine Island and Thwaites Glaciers, respectively.

Figure 8a and b show corresponding profiles measured in two differential interferograms of the eastern tongue of Thwaites Glacier. The profile location and the measured quadruple tidal amplitude along the profile are shown in the left and right sub-panels of the figure, respectively. The profile with the larger quadruple tidal difference of 0.4 m (Fig. 8a) is matched accurately by Equation (1). The fitted grounding-line position $x_{\mathrm{gl}} =$ 3.3 km and the flexural parameter $\beta = 0.63 \times 10^{-3}\,\mathrm{km}^{-1}$, can be taken as proxies of the actual values. Fitting the elastic-beam model to the profile of Figure 8b with a quadruple tidal amplitude of 0.03 m produces $x_{\mathrm{gl}} = 4.5$ km. The resulting misplacement of $\Delta x_{\mathrm{gl}} =$ 1.2 km cannot be easily recognized by eye without comparing to Figure 8a.

Figure 8c and d show corresponding profiles measured in two differential interferograms of the central part of Pine Island Glacier. Both of these interferograms were part of a study by Rignot (1998a). The profile of Figure 8c with a large quadruple tidal amplitude (−0.32 m) is again fitted well with the elastic-beam model. The grounding line is detected at $x_{\mathrm{gl}} = 3.2$ km. In contrast, the Figure 8d profile with a quadruple tidal amplitude of 0.085 m shows a peculiar hump-shaped forebulge that cannot be explained by the elastic-beam model. In terms of Equations (12), the grounding line in this case is even more severely misplaced than in Figure 8b, with the elastic-beam model describing only the outer part of the profile seaward of the top of the forebulge (the corresponding tidal amplitude is inverted with respect to the true one). In terms of interactive grounding-line detection, this category of misplacement is, however, less critical than that of Figure 8b. Despite the anomalous shape, the zone of concentrated flexure starts close to the true grounding line, and fitting Equation (1) there avoids the gross misplacement (this has been done in Figure 8d). The anomalous shape will nevertheless compromise the accuracy of the fit parameters x_{gl} and β. For Figure 8c and d we additionally show curves of the viscoelastic-beam model (Lingle and others, 1981). The observed profile shapes cannot be explained with this model.

In the following we analyze the range of tidal combinations and tidal sensitivities of the grounding line that can explain the profiles of Figure 8b and d. As mentioned before, the observed deviations from the elastic-beam model in the vicinity of the true grounding line are due to less than four SAR scenes contributing to the tidal phase contribution in this

https://doi.org/10.3189/172756502781831197 Published online by Cambridge University Press

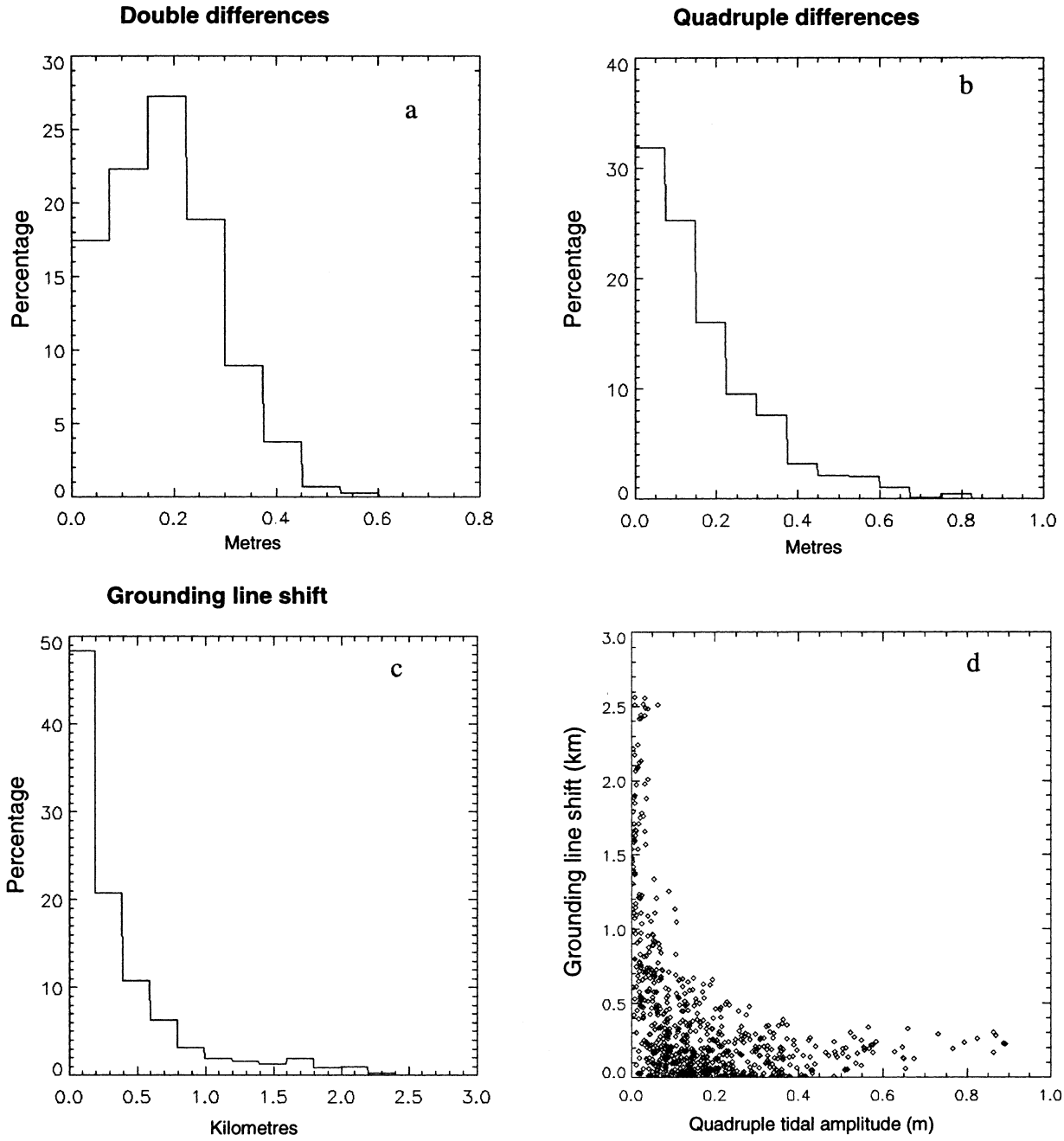

Fig. 7. Simulation with FES95.2 model tide values of a 2 year period. Shown are corresponding histograms of double (a) and quadruple (b) tidal differences, as well as absolute value of grounding-line shift (c). Parameters used in the simulation are $\beta = 0.6\,\mathrm{km}^{-1}$ and $f = 300$. The actual distribution of grounding line with quadruple tidal difference is shown in (d).

range. In the analysis we use a generalized version of Equation (7) that takes this effect into account. We assume the mean sea-level grounding line at $x_{\mathrm{msl}} = 3.3$ and 3.2 km, respectively. A general tide-quadruple $[\Delta w_1, \Delta w_2, \Delta w_3, \Delta w_4]$ can be parameterized as

$$\begin{pmatrix} \Delta w_1 \\ \Delta w_2 \\ \Delta w_3 \\ \Delta w_4 \end{pmatrix} = \begin{pmatrix} a \\ ad \\ -ad \\ -a \end{pmatrix} + \frac{c}{4} \begin{pmatrix} 1 \\ -1 \\ -1 \\ 1 \end{pmatrix} + s \qquad (13)$$

with

$$\begin{aligned} a &= \frac{\Delta w_1 - \Delta w_4}{2}\,, \quad d = \frac{\Delta w_2 - \Delta w_3}{\Delta w_1 - \Delta w_4}\,, \\ c &= \Delta w_1 - \Delta w_2 - \Delta w_3 - \Delta w_4\,, \\ s &= \frac{\Delta w_1 + \Delta w_2 + \Delta w_3 + \Delta w_4}{4}\,. \end{aligned} \qquad (14)$$

An additional free parameter is f, which leads to an overall five-dimensional parameterization of Equation (7). Two of the parameters, the quadruple tidal amplitude c measured between x_{msl} and infinity and the mean tide level s, are determined by the boundary conditions. From the interferometric profiles we find $c = 0.0195$ m and $s \cdot f = 0.12$ km for the case of Figure 8b. For Figure 8d we analogously find $c = 0.083$ m and $s \cdot f = 1.23$ km. The quantity $s \cdot f$ describes the shift of the grounding line at mean tide level s with respect to x_{msl}; it is fixed by using x_{gl} from Figure 8a and c as proxy values for x_{msl}. To find a solution for the remaining three parameters, we vary a and d within reasonable limits on a regular grid ($a \in [-1.8\,\mathrm{m}, 1.8\,\mathrm{m}]$, $d \in [0.3, 0.99]$) and then fit Equation (7) with respect to f. Figure 9 shows the degenerated parameter solutions for the best fit of Equation (7) to the interferometric profiles in Figure 8b and d (dashed lines there). The left panels of the figure show how d is related to a; the corresponding values of f are shown in the right panels. For realis-

https://doi.org/10.3189/172756502781831197 Published online by Cambridge University Press

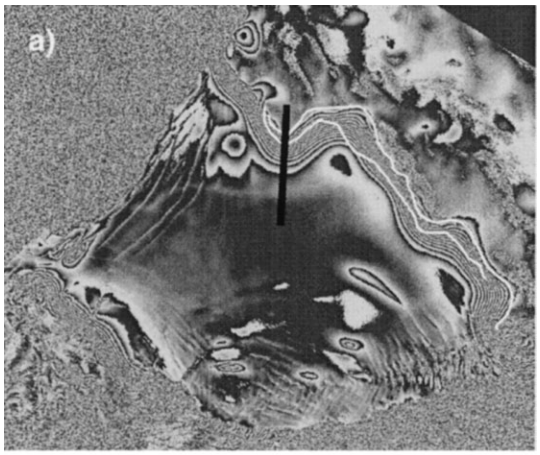

Thwaites-East Glacier

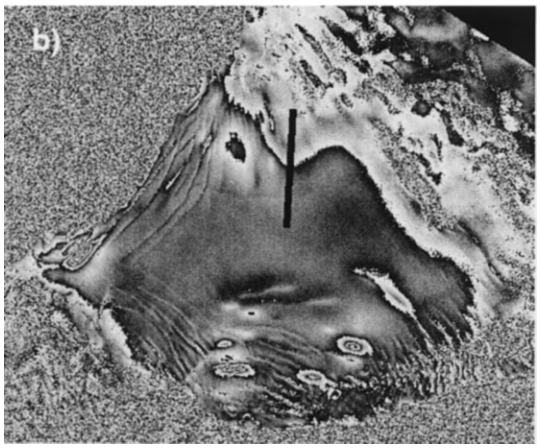

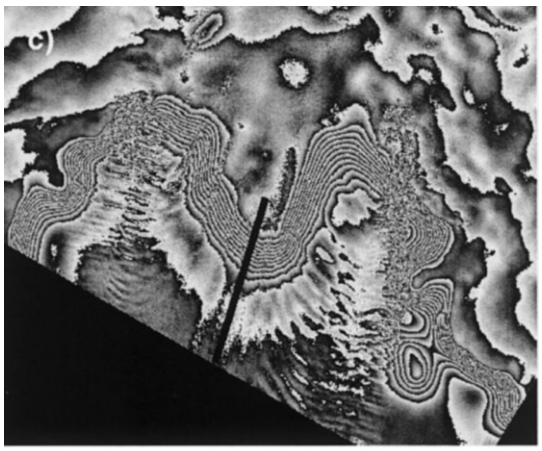

Pine Island Glacier

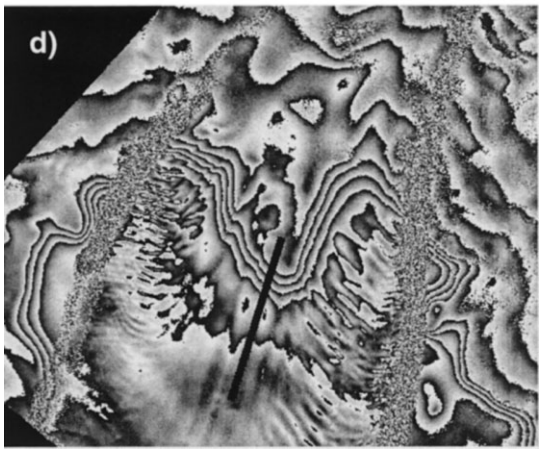

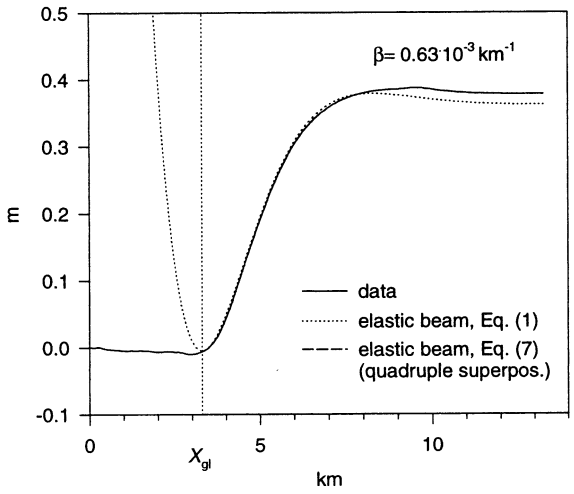

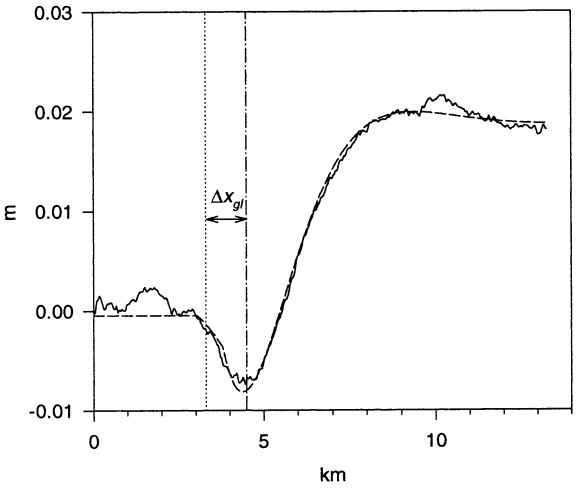

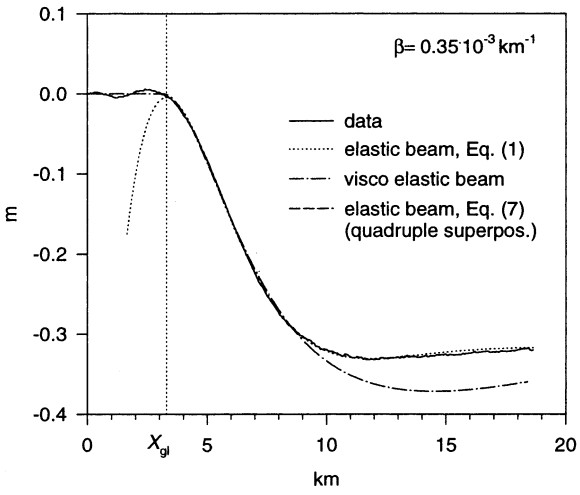

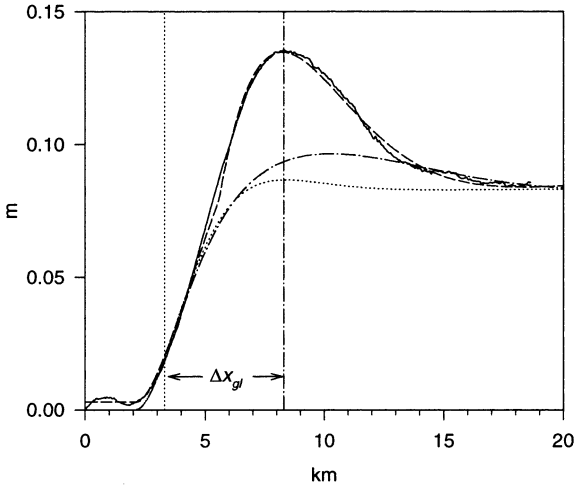

https://doi.org/10.3189/172756502781831197 Published online by Cambridge University Press

Fig. 8 (opposite). Differential interferometric profiles across the tidal flexing zones of Thwaites east (a, b) and Pine Island (c, d) Glaciers. The left side of each sub-figure shows the location of the chosen profile marked as a black bar in the corresponding differential interferogram. The right side shows measured phase data along the profile in metres. (a) and (c) show examples with large tidal amplitudes that allow correct derivation of β and $x_{\mathrm{gl}} \approx x_{\mathrm{msl}}$ (dotted vertical line). Best fits with the elastic-beam model are superimposed. In contrast, (b) and (d) have small tidal amplitudes and anomalous shapes. Apparent grounding-line shifts derived from fitting Equation (1) are $\Delta x_{\mathrm{gl}} = 1.2$ and 5.0 km, respectively. Best fits for quadruple tidal profiles with Equation (7) are superimposed. Vertical dash-dotted line: apparent grounding-line position. For Pine Island Glacier (c, d), fit curves are shown for both elastic- and viscoelastic-beam model using β found from the elastic-beam best fit in (c). For Thwaites east Glacier, grounding lines detected continuously with Equation (1) in differential interferograms (a) and (b) are marked as white lines in interferogram (a).

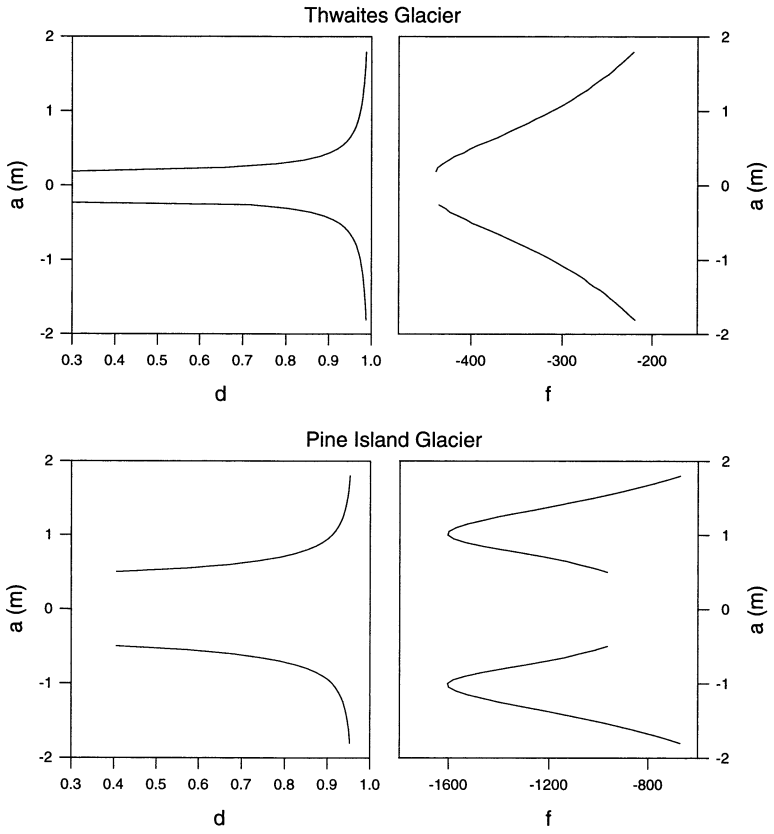

Fig. 9. Valid parameterizations (Equation (13)) for the best-fit quadruple tidal profiles shown as dashed curves in Figure 8b and d. For both the Pine Island and the Thwaites (east) Glacier example we show plots of parameters a vs d (left side) as well as a vs f (right side).

tic tide levels 0.3 m $> |a| <$ 2.0 m we find $-200 < f < -450$ for Figure 8b and $-1600 < f < -650$ for Figure 8d. Analyses of other cases with large Δx_{gl} sampled in Figure 7 show that the presented results can be generalized.

In summary, the tidal phase contribution in a differential interferogram generally corresponds to a 1-D manifold of possible quadruple combinations of single tide levels and f values. For large Δx_{gl}, the tidal shift of the grounding line f is relatively insensitive to a wide range of tide levels a. Under this condition tide data with a relatively low degree of accuracy would be sufficient to determine f and, if surface slope is known, also the basal slope α_{B} (Equation (8)).

DISCUSSION

For single interferograms, grounding-line detection is possible only for regions of low ice-velocity gradient. Differential interferograms get rid of this limitation by removing the phase contribution due to continuous horizontal motion (Rignot, 1998b). However, in the previous section we have shown that this advantage comes at a price: for quadruple tide levels smaller than about 10% of the tide dynamics, there is the possibility of making a gross error when locating the grounding line with the elastic-beam model. Independent tide data, measured or modelled, are necessary to correct this problem.

In the following we explain why grounding-line detection in a single interferogram, in regions of small ice-velocity gradients where it can be accomplished, is more robust. The parameterization of the tide couple $[\Delta w_1, \Delta w_2]$ making up a single interferogram

$$\begin{pmatrix} \Delta w_1 \\ \Delta w_2 \end{pmatrix} = \frac{c}{2} \begin{pmatrix} 1 \\ -1 \end{pmatrix} + s \qquad (15)$$

with

$$c = \Delta w_1 - \Delta w_2\,, \quad s = \frac{\Delta w_1 + \Delta w_2}{2} \qquad (16)$$

has two parameters fewer than that of a differential interferogram (Equations (13) and (14)). The superposition of tidal flexure profiles is described by Equations (7–9) with S_2 replacing S_4 everywhere. Again, the parameter c is the tidal amplitude in the interferogram. However, in contrast to the differential case the parameter $s \cdot f$ can now be fitted unambiguously without assuming the approximate location of the mean sea-level grounding line x_{msl}. Fitting $s \cdot f$ fixes both x_{msl} and the shape of the fit simultaneously. If the profile in Figure 8b were from a single interferogram, we would find $s \cdot f =$ 1.8 km,

https://doi.org/10.3189/172756502781831197 Published online by Cambridge University Press

which locates x_{msl} unambiguously at 3.3 km − 1.8 km = 1.5 km. Turned around, single interferograms with small tidal phase contribution are less likely to exhibit false grounding-line shifts than corresponding differential interferograms.

This result supports Metzig and others' (1997) derivation of a significant 4.5 km tidal shift of the grounding line of Schirmacheroasen ice shelf, Antarctica, by comparing two single interferograms. It is not possible to produce both a 4.5 km grounding-line misplacement and the observed phase-profile shapes with Equations (15) and (16). For both phase-profile shapes, f must be small, corresponding to steep surface or bottom slope (Equation (8)). Apparently contrary values of $f > 3000$ evaluated from an independently measured tide-level difference of 1.5 m must be due to an ice plain in between the single interferometric grounding lines (representing high and low tide conditions, respectively). Due to the complications described in the previous section, drawing the same conclusions from two corresponding differential interferograms would be considerably less robust.

CONCLUSION

Grounding-line location detected with the elastic-beam model is strictly valid only for a straight grounding line and a homogeneous ice shelf of constant thickness. The elastic-beam model produces a good approximation of grounding-line location (on the 100 m level) for seaward protrusions (convex, positive curvature) of the grounding line down to scales of one ice thickness or less. The same is true for any realistic seaward decrease of shelf-ice thickness. On the other hand, comparable negative curvatures present in embayments of the grounding line lead to considerably larger grounding-line misplacement. We conclude that, judged from grounding-line geometry, studies of the shift of grounding-line location over time may include regions of larger positive curvature without requiring methods more sophisticated than the elastic-beam model. Regions with larger negative curvature of the grounding line should be excluded.

For differential interferograms, there is a non-vanishing probability of making severe errors when locating the grounding line with the elastic-beam model. The problem is restricted to small quadruple tide levels[2], which are roughly below 10% of the dynamics of individual tide levels. If this condition is met, grounding-line misplacements up to several kilometres are possible. About 20% of all tidal combinations will produce such large misplacements. Grounding-line detection in single interferograms, within their reduced range of applicability (regions of small ice-velocity gradient), does not show a comparable possibility of error. This makes the interpretation of a single interferogram with small tidal phase contribution less ambiguous than that of a corresponding differential interferogram.

ACKNOWLEDGEMENTS

We are grateful for continued support by the German Remote Sensing Centre (DFD-DLR). Particular thanks go to K. Reiniger and his team for processing the ERS SAR data and M. Eineder and his team for providing support on the interferometric processing system GENESIS. Comments by H. Rott on an earlier version of the manuscript, as well as scientific editing by T. A. Scambos and the comments of T. J. Hughes and an anonymous reviewer, helped to improve the manuscript.

REFERENCES

Allen, C. T. S., S. Gogineni, B. Wohletz, K. Jezek and T. S. Chuah. 1997. Airborne radio echo sounding of outlet glaciers in Greenland. *Int. J. Remote Sensing*, **18**(14), 3103–3107.

Anandakrishnan, S. and R. B. Alley. 1997. Tidal forcing of basal seismicity of Ice Stream C, West Antarctica, observed far inland. *J. Geophys. Res.*, **102**(B7), 15,183–15,196.

Crabtree, R. D. and C. S. M. Doake. 1982. Pine Island Glacier and its drainage basin: results from radio-echo sounding. *Ann. Glaciol.*, **3**, 65–70.

Doake, C. S. M. 1992. Gravimetric tidal measurement on Filchner Ronne Ice Shelf. *In* Oerter, H., *ed. Filchner–Ronne Ice Shelf Programme. Report No. 6 (1992)*. Bremerhaven, Alfred Wegener Institute for Polar and Marine Research, 34–39.

Echelmeyer, K. and W. Harrison. 1989. Dynamics of Jakobshavns ice stream, West Greenland. [Abstract.] *Ann. Glaciol.*, **12**, 201.

Goldstein, R. M., H. Engelhardt, B. Kamb and R. M. Frolich. 1993. Satellite radar interferometry for monitoring ice sheet motion: application to an Antarctic ice stream. *Science*, **262**(5139), 1525–1530.

Hartl, P., K.-H. Thiel, X. Wu, C. S. M. Doake and J. Sievers. 1994. Application of SAR interferometry with ERS-1 in the Antarctic. *Earth Obs. Q.*, **43**, 1–4.

Hughes, T. 1977. West Antarctic ice streams. *Rev. Geophys. Space Phys.*, **15**(1), 1–46.

Kertz, W. 1992. Einführung in die Geophysik I. *BI-Hochschultaschenbuch*, **275**, 110–115.

Kirchhoff, G. 1850. Über das Gleichgewicht und die Bewegung einer elastischen Scheibe. *Crelles J.*, **40**, 51–88.

le Provost, C., F. Lyard, J. M. Molines, M. L. Genco and F. Rabilloud. 1997. A hydrodynamic ocean tide model improved by assimilating a satellite altimeter derived dataset. *J. Geophys. Res.*, **103**(C3), 5513–5529.

Lingle, C. S., T. J. Hughes and R. C. Kollmeyer. 1981. Tidal flexure of Jakobshavns glacier, West Greenland. *J. Geophys. Res.*, **86**(B5), 3960–3968.

Metzig, R., R. Dietrich, W. Korth, J. Perlt, R. Hartmann and W. Winzer. 2000. Horizontal ice velocity estimation and grounding zone detection in the surroundings of Schirmacheroase, Antarctica, using SAR interferometry. *Polarforschung*, **67**(1–2), 1997, 7–14.

Paterson, W. S. B. 1994. *The physics of glaciers. Third edition.* Oxford, etc., Elsevier.

Rignot, E. J. 1998a. Fast recession of a West Antarctic glacier. *Science*, **281**(5376), 549–551.

Rignot, E. 1998b. Hinge-line migration of Petermann Gletscher, north Greenland, detected using satellite-radar interferometry. *J. Glaciol.*, **44**(148), 469–476.

Smith, A. M. 1997. Variations in basal conditions on Rutford Ice Stream, West Antarctica. *J. Glaciol.*, **43**(144), 251–261.

Thomas, R. H. 1979. The dynamics of marine ice sheets. *J. Glaciol.*, **24**(90), 167–177.

MS received 3 September 2001 and accepted in revised form 29 April 2002

[2]Quadruple tide level is the (1–2) − (3–4) difference of the four individual tide levels at the times of the SAR scenes composing the differential interferogram.